

Microscopic modeling of transverse mode instabilities in mode-locked vertical external-cavity surface-emitting lasers

Cite as: Appl. Phys. Lett. **116**, 031102 (2020); <https://doi.org/10.1063/1.5134070>

Submitted: 29 October 2019 . Accepted: 07 January 2020 . Published Online: 21 January 2020

S. McLaren , I. Kilen , and J. V. Moloney 



View Online



Export Citation



CrossMark

ARTICLES YOU MAY BE INTERESTED IN

[Dirac energy spectrum and inverted bandgap in metamorphic InAsSb/InSb superlattices](#)

Applied Physics Letters **116**, 032101 (2020); <https://doi.org/10.1063/1.5128634>

[4Pi multiphoton polymerization](#)

Applied Physics Letters **116**, 031101 (2020); <https://doi.org/10.1063/1.5128786>

[High operating temperature InAsSb-based mid-infrared focal plane array with a band-aligned compound barrier](#)

Applied Physics Letters **116**, 031104 (2020); <https://doi.org/10.1063/1.5133093>

Hall Effect Measurement Handbook

A comprehensive resource for researchers

Explore theory, methods, sources of errors, and ways to minimize the effects of errors



Microscopic modeling of transverse mode instabilities in mode-locked vertical external-cavity surface-emitting lasers

Cite as: Appl. Phys. Lett. **116**, 031102 (2020); doi: [10.1063/1.5134070](https://doi.org/10.1063/1.5134070)

Submitted: 29 October 2019 · Accepted: 7 January 2020 ·

Published Online: 21 January 2020



View Online



Export Citation



CrossMark

S. McLaren,^{1,2,a)}  I. Kilen,^{2,3}  and J. V. Moloney^{1,2,3,4} 

AFFILIATIONS

¹Program in Applied Mathematics, University of Arizona, 617 N. Santa Rita Ave., Tucson, Arizona 85721, USA

²Arizona Center for Mathematical Sciences, University of Arizona, 1630 East University Blvd., Tucson, Arizona 85721, USA

³Wyant College of Optical Sciences, University of Arizona, 1630 East University Boulevard, Tucson, Arizona 85721, USA

⁴Department of Mathematics, University of Arizona, 617 N. Santa Rita Ave., Tucson, Arizona 85721, USA

^{a)}Electronic mail: smclaren@math.arizona.edu

ABSTRACT

The generation and control of higher order transverse modes within a mode-locked vertical external-cavity surface-emitting laser with a semiconductor saturable absorber mirror are studied using a numerical solver for the two dimensional Maxwell Semiconductor Bloch Equations. In this work, the complex spatiotemporal evolution of the pulse toward a mode-locked state depends sensitively on the pumping level and pump to pulse spot size ratio. Microscopic physics sourced effects such as kinetic hole burning and filling, occurring on femtosecond timescales, play a central role. In particular, unsaturated charge carriers, both spectrally and transversally, initiate the development of asymmetric pulse profiles that transform over various characteristic time scales in a carrier chasing behavior.

Published under license by AIP Publishing. <https://doi.org/10.1063/1.5134070>

Vertical external-cavity surface-emitting lasers (VECSELs) are promising compact sources for low noise, high-power, and ultrafast pulses with excellent beam quality and flexibility offered by an external cavity.^{1–3} These lasers are typically optically pumped and consist of a multilayered semiconductor gain structure. In order to achieve mode-locking, a semiconductor saturable absorber mirror (SESAM) can be introduced. The wide wavelength tunability, achieved through bandgap engineering of the semiconductor heterostructures, has allowed these lasers to emerge as the most versatile new laser platform with applications ranging from manufacturing, life sciences, spectroscopy, and optical frequency comb generation.^{4,5}

There is significant interest in pulse stability and the formation of unstable pulses within these lasers.^{6–8} There is also a recent focus on the generation of higher order modes, as a platform for optical vortices, among other applications.^{9,10} In both cases, it is necessary to understand how higher order transverse modes fluctuate within these systems. This paper utilizes a microscopic based many-body model of a VECSEL cavity to explore how ultrafast kinetic spectral hole burning and filling interacts with transverse degrees of freedom to influence femtosecond mode-locked single

and multiple pulse dynamics. Utilizing different pulse to pump spot size ratios, w_0/w_p , we observe how the momentum integrated spectral holes dynamically feed the background charge carrier density n_0 to either stabilize or destabilize the transverse signal beam profile. On these ultrafast timescales, unsaturated high and low momentum carriers outside of these spectral holes provide additional gain to break overall symmetry.

There exist numerous numerical models to characterize VECSELs, which capture the corresponding physics at various levels of accuracy. A classical model is based on macroscopic rate equations with prescribed gains and losses.¹¹ One can also describe the cavity gain and loss using ordinary differential equations¹² or delay differential equations (DDEs).¹³ For pulses on the order of tens of picoseconds, it is usual to adiabatically eliminate the polarization, leading to an optical susceptibility, which can be analytically approximated.¹⁴ These models are computationally simpler, provide great insight, and open up some very interesting windows for the application of dynamical systems. However, these approaches do not capture the intricate non-equilibrium dynamics of the system on the scale of sub-picosecond pulses. These dynamics arise from the inhomogeneous depletion of

inverted charge carrier populations away from Fermi distributions. It has been shown that this effect deforms the instantaneous gain in a nonlinear manner, such that similar initial gain profiles can lead to drastically different modelocking behaviors.¹⁵ In order to study how these microscopic effects influence the pulse, we model the system from a microscopic perspective.

The current model, the Maxwell Semiconductor Bloch Equations (SBEs), couples macroscopic wave propagation to the induced microscopic polarization within the semiconductor structure. The core of the model is the Semiconductor Bloch Equations (SBEs), which describe the polarization response of the charge carriers, confined within semiconductor quantum wells (QWs), to an applied electric field.¹⁶

$$\begin{aligned} \frac{\partial}{\partial t} p_k &= -i\omega_k p_k - i\Omega_k (n_k^e + n_k^h - 1) + \Lambda_{spont}^p + \left. \frac{\partial}{\partial t} p_k \right|_{scat}, \\ \frac{\partial}{\partial t} n_k^{e(h)} &= i[\Omega_k p_k^* - \Omega_k^* p_k] + \Lambda_{spont}^n + \left. \frac{\partial}{\partial t} n_k^{e(h)} \right|_{scat}. \end{aligned}$$

Therein, p_k is the microscopic polarization and $n_k^{e(h)}$ are the occupation numbers for electrons (holes), for momentum state k . The two band parabolic particle energies, $\hbar\omega_k$, and Rabi frequency, Ω_k , are renormalized, in the Hartree–Fock limit, by the screened Coulomb potential matrix, V_k , and the spontaneous emission terms are functions of the product $n_k^e n_k^h$, as described in previous work.¹⁷

It has been shown previously that for ultrafast pulses, on the order of 100 fs, carrier scattering can be well approximated by relaxing carriers toward a dynamic Fermi distribution based on instantaneous densities and temperatures.¹⁵ The QW carrier replenishment from barrier pumping will be modeled by relaxing toward a constant Fermi distribution at the pump density and lattice temperature. These processes influence the pulse on two very different timescales. The fast carrier scattering transports energy into the spectral region of the pulse on a hundred femtosecond characteristic time scale, while the much slower carrier replenishment determines the overall mode-locked QW density with a characteristic time scale of several tens of picoseconds. Thus, we approximate

$$\left. \frac{\partial}{\partial t} p_k \right|_{scat} = -\frac{1}{\tau_{deph}} p_k, \quad (1)$$

$$\left. \frac{\partial}{\partial t} n_k^{e(h)} \right|_{scat} = -\frac{1}{\tau_{scat}} \left(n_k^{e(h)} - f_k^{e(h)} \right) - \frac{1}{\tau_{fill}} \left(n_k^{e(h)} - F_k^{e(h)} \right), \quad (2)$$

where $f_k^{e(h)}$, $F_k^{e(h)}$ are Fermi distributions, the former computed based on initial temperatures and densities and the latter based on instantaneous values. The dephasing and kinetic hole filling rates were taken as $\tau_{deph} = 47fs$ and $\tau_{fill} = 100fs$. The scattering rates were taken as $\tau_{scat,g} = 30ps$ and $\tau_{scat,a} = 2ps$ for the gain and absorber QWs, respectively. These rates were approximated from single-pass simulations, which treat the carriers at the Second-Born Markov level, and show excellent agreement with experiments.¹⁵

These equations describe an updated scheme for the microscopic polarization induced by an electric field, $E(x, z, t)$. Integrating the microscopic states gives the macroscopic polarization, $P(x, z, t) = \sum d_{cv} p_k + c.c.$, which is used to update the electric field propagation equation,

$$\left(\Delta - \frac{n(z)^2}{c_0^2} \frac{\partial^2}{\partial t^2} \right) E(x, z, t) = \mu_0 \frac{\partial^2}{\partial t^2} P(x, z, t), \quad (3)$$

for physical constants μ_0, c_0 and our piecewise constant refractive index $n(z)$, where, outside of our QWs, we assume linear dispersion. The linear simulation domain consists of a gain structure, a resonator cavity, and a saturable absorber. The model gain structure consists of a 61 layer AlGaAs-AlAs distributed Bragg reflector (DBR), a 10 QW resonant periodic gain (RPG) structure of 8 nm AlGaAs QWs, a bilayer antireflective (AR) coating of Ta₂O₅ and SiO₂, and an InGaP cap layer. The transverse discretization of the SBE makes modeling each QW separately computationally demanding. As an approximation, we use a single effective QW, placed to optimally replicate a one dimensional simulation utilizing the full structure. The SESAM consists of an AR coating of Si₃N₄, a single unpumped QW, and a partially reflecting back mirror, $R = 0.99\%$.

Figure 1 shows the initial carrier density pump profile, a Super-Gaussian profile with a spot size of $w_p = 336 \mu m$, along with a numerically obtained temperature profile.¹⁸ The given density profile has a peak density of $n_0 = 2.35 \times 10^{16} m^{-2}$ and a background density of $n_b = 5.0 \times 10^{14} m^{-2}$. These profiles were modified for studying various pulse to pump spot size ratios.

The resonator consists of two air regions, $L_1 = 49.054 mm$, $L_2 = 6.622 mm$, separated by a lens, $f = 6.1936 mm$, and is designed for stable operation for the prescribed spot sizes. Pulse propagation is numerically integrated using a pseudo-spectral propagator and a phase mask for the lenses.^{19,20} In general, the cavity length delays the pulse interaction with the QWs and is chosen appropriately to produce a desired stable mode-locked pulse. From the SBE, it is clear that the process with the longest time scale is the carrier replenishing, which brings the QW density toward the background density. To facilitate stable single pulse modelocking with the given cavity setup, we will use a relatively short round trip time, $T_{rt} = 22ps$, which allows us to

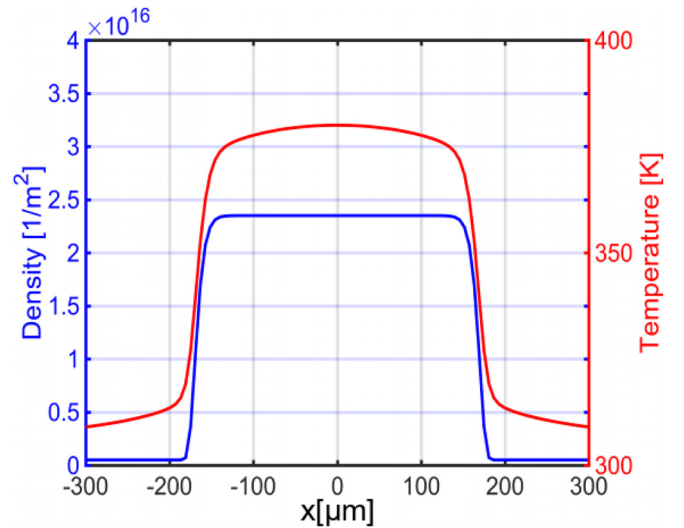


FIG. 1. Super-Gaussian pump profile with a spot size of $w_p = 336 \mu m$ used along with a numerically obtained temperature profile.

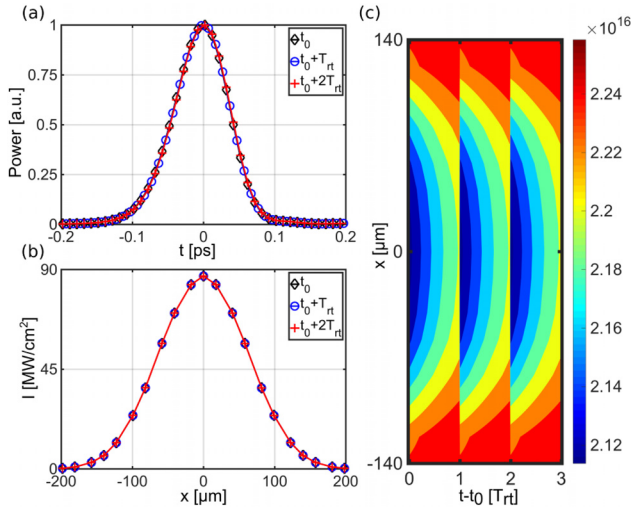


FIG. 2. Stable fundamental mode operation over three successive round trips after a simulation time of $t_0 = 148$ ns. (a) The integrated transverse pulse intensity, (b) transverse profile at the pulse peak, and (c) total charge carrier density.

capture essential microscopic QW physics without an excessive computational burden.

Plotted in Fig. 2 are three consecutive round trips for a converged stable fundamental mode-locking simulation with a pulse to pump spot size ratio of $w_0/w_p = 0.6$ and a peak pump carrier density of $n_0 = 2.35 \times 10^{16} \text{ m}^{-2}$ after a simulation time of $t_0 = 148$ ns. Figure 2(a) shows the integrated transverse pulse intensity as a function of time and Fig. 2(b) shows the transverse pulse intensity at its peak, which demonstrate temporal and transverse stabilities. Figure 2(c) shows the total carrier density over these round trips derived from the momentum integrated nonequilibrium distributions.

As the pulse enters the pumped QW, carriers recombine to burn a deep kinetic hole. For fundamental mode-locked operation, these

kinetic holes are consistently burned symmetrically about the same spectral center and over thousands of round trips, a stable pattern of hole burning and filling emerges.

Previous work on continuous wave (CW) operation has shown that for a given absorbed power, 18 W, the ratio $w_0/w_p = 0.75$ is a transition point between single and multi-mode CW operation.¹⁸ Figure 2 shows that with the fully microscopic considerations, we can obtain mode-locked fundamental transverse mode operation at lower ratios, $w_0/w_p = 0.6$. Because kinetic holes burned by the pulse do not fully recover between passes, they further diminish the gain along the wings, limiting the growth of higher order modes and stabilizing the cavity.

For large enough pumping levels, inversion bleaching at the spectral center of the fundamental mode occurs, and we expect multiple pulses to form within the cavity. Figure 3 shows a single round trip of an unstable multi-pulsing result, for the same pump to spot size ratio, $w_0/w_p = 0.6$, with a significantly higher background carrier density of $n_0 = 3.5 \times 10^{16} \text{ m}^{-2}$ after a simulation time of $t_0 = 115$ ns. The integrated transverse intensity, Fig. 3(a), shows four distinct pulses present within a single pass. The transverse profiles of the pulses, Fig. 3(b), exhibit strong spatiotemporal fluctuations characteristic of higher order mode behavior. These data are recorded when the dynamics have reached an asymptotic state well after the total energy in the cavity has stabilized. Figure 3(d) shows the population inversion, $n_k^e + n_k^h - 1$, 500 fs before the $t = t_0$ pulse enters the QW. Because the kinetic hole filling rate, $\tau_{fill} = 100$ fs, is fast relative to the time between pulses, the carriers attain quasi-Fermi distributions with depleted densities between pulse interactions. At the same time, the slower carrier replenishment, $\tau_{scat,g} = 30$ ps, has established a non-equilibrium energy balance that maintains several propagating cavity pulses in the cavity. Naturally, the pulses cannot be sustained from the same carrier reservoir and thus extract carriers non-uniformly from the total available reservoir. 100 fs after the peak of this first sub-pulse, shown in Fig. 3(e), the pulse has burned an asymmetric kinetic hole, which feeds back into the corresponding transverse carrier density in Fig. 3(c). In Fig. 3(f), 500 fs before the next pulse comes in, at $t = t_0 + 4$ ps, the

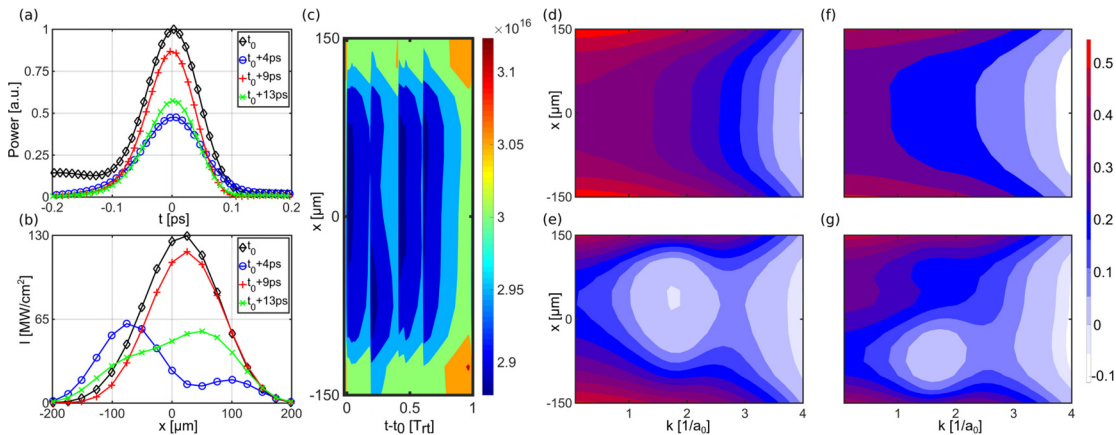


FIG. 3. Unstable high density operation with multiple pulse formation over a single round trip, $t_0 = 115$ ns with $w_0/w_p = 0.6$ and $n_0 = 3.5 \times 10^{16} \text{ m}^{-2}$. (a) Integrated transverse intensity hints at fundamental Gaussian operation. (b) Transverse intensity profiles at the pulse peak and (c) total carrier density show the presence of higher order transverse modes. (d) Population inversions 500 fs before and (e) 100 fs after the $t = t_0$ pulse shows kinetic hole burning about the pulse's spectral and transverse centers. (f) The recovered population inversion, 500 fs before the next pulse, at $t = t_0 + 4$ ps comes in. (g) 100 fs after the pulse peak, it has burned a spectrally, and transversally, distinct kinetic hole.

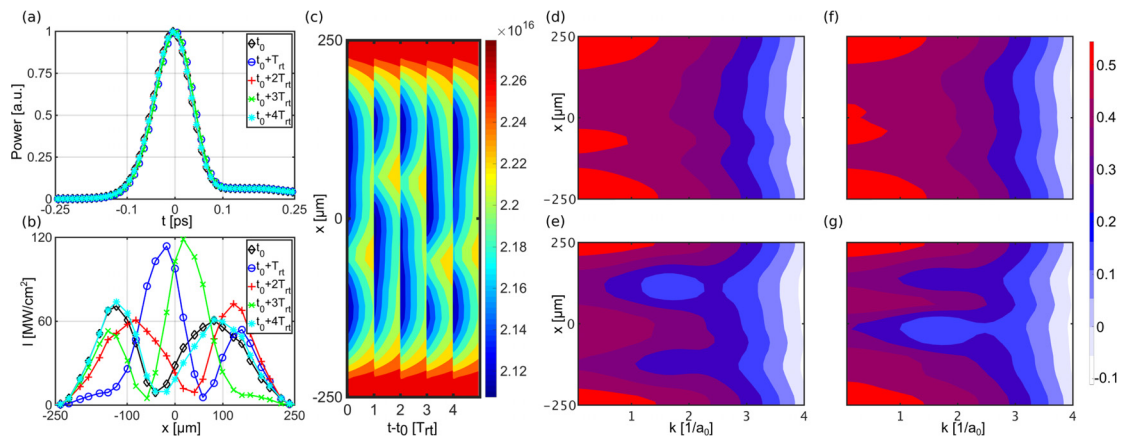


FIG. 4. Five successive round trips under unstable wide pump operation after a simulation time of $t_0 = 380$ ns with $w_0/w_p = 0.3$ and $n_0 = 2.35 \times 10^{16} \text{ m}^{-2}$. (a) Integrated transverse intensity indicating stable pulse power. (b) Transverse profiles at the peak of the pulse and (c) the total carrier density, showing periodic profile oscillations. (d) Population inversions 500 fs before and (e) 100 fs after the $t = t_0$ pulse shows kinetic hole burning about the pulse's spectral and transverse centers. (f) 500 fs before the next pass, at $t_0 + T_{rt}$, the inversion recovers to a different homogeneous state. (g) 100 fs after the peak of the pulse, it has burned a distinct kinetic hole in the inversion.

carriers shown in Fig. 3(e) have partially recovered back to different quasi-Fermi distributions. At the peak of the second sub-pulse, shown in Fig. 3(g), the kinetic hole distribution is strongly displaced off-axis reflecting the strong asymmetry in the corresponding transverse beam profile in Fig. 3(b). Consequently, the total carrier densities arise from highly nontrivial momentum integrated nonequilibrium distributions.

We finally explore a different physical scenario where it appears that a fundamental mode-locked pulse displays conservation of power but exhibits near cyclic and large transverse beam fluctuations. Figure 4 shows five consecutive round trips of an unstable single pulse simulation after a simulation time of $t_0 = 380$ ns. The simulation used a widened pulse to pump spot size ratio, $w_0/w_p = 0.3$ and an initial carrier density reduced to $n_0 = 2.35 \times 10^{16} \text{ m}^{-2}$. Figure 4(a) shows integrated transverse pulse intensities, which again point toward stable fundamental mode operation. However, the transverse profile at the pulse peak for each of these round trips, Fig. 4(b), shows strong transverse beam fluctuations. The pulse profile shifts about the origin on successive round trips, approximately returning to its original shape after four consecutive passes. To explain this result, we again look at the population inversion. Shown in Fig. 4(d) for 500 fs before the $t = t_0$ pulse hits the QW, the inversion is in an inhomogeneous state, reflecting the fact that the carriers have not fully recovered. The pulse burns a kinetic hole in the inversion, shown in Fig. 4(e) for 100 fs after the pulse. Because the time between pulse interactions is a full round trip, the carriers can more fully recover toward their initial states. However, the non-equilibrium pulse shape is strongly deformed because the wider pump spot significantly expands the available carrier reservoir. Any inverted carriers that were not extracted by the main pulse will amplify the pulse wings, enabling complex pulse shapes to be maintained in the transverse dimension. Figure 4(f) shows the recovered inversion, 500 fs prior to the pulse returning on the next round trip, $t = t_0 + T_{rt}$, which is significantly different from the previous pass. Figure 4(g) shows the inversion 100 fs after the peak of the returned pulse and depicts a kinetic hole burned at a different transverse location, shifted by the microscopic variations accumulated over the previous round trip. The burning of kinetic holes depletes carriers and,

when integrated, leads to visible shifts in total carrier density. Figure 4(c) shows the total carrier density over the five round trips, as integrated over the carrier distributions, and highlights how the microscopic nonequilibrium dynamics drive the macroscopic behavior of the system.

In summary, the nonlinear interactions of transverse macroscopic and microscopic effects within a VECSEL cavity are shown to produce both stabilizing and destabilizing behaviors. Low ratios of pulse to pump spot sizes, $w_0/w_p \geq 0.6$, are shown to be capable of leading to high beam quality. However, this ratio by itself is not a sufficient control to guarantee fundamental operation. Pump levels within the quantum wells must also be maintained, to avoid the formation and aperiodic oscillations of secondary pulses and higher order transverse modes. These instabilities arise through inhomogeneous kinetic hole burning and filling along both the spectral and transverse axes. Unstable pulse profiles chase peak carrier densities along the two axes, transforming dramatically on successive, and over hundreds of, round trips. This behavior can persist even without significant fluctuation in output power. Thus, careful control of these mechanisms, measurements of the transversally resolved pulse intensity, and microscopically based simulations are vital for a full understanding of how to control the growth of higher-order transverse modes and secondary pulses.

This material is based upon the work supported by the Air Force Office of Scientific Research under Grant No. FA9550-17-1-0246 and the National Defense Science & Engineering Graduate Fellowship (NDSEG) Program.

REFERENCES

- ¹A. Rahimi-Iman, "Recent advances in VECSELs," *J. Opt.* **18**, 093003 (2016).
- ²A. C. Tropper, A. H. Quarterman, and K. G. Wilcox, "Ultrafast vertical-external-cavity surface-emitting lasers," in *Advances in Semiconductor Lasers*, edited by J. J. Coleman, A. C. Bryce, and C. Jagadish (Elsevier Inc., 2012), Chap. 7, Vol. 86.
- ³B. W. Tilma, M. Mangold, C. A. Zaugg, S. M. Link, D. Waldburger, A. Klenner, A. S. Mayer, E. Gini, M. Golling, and U. Keller, "Recent advances in ultrafast semiconductor disk lasers," *Light: Sci. Appl.* **4**, e310 (2015).

- ⁴M. Guina, A. Rantamäki, and A. Härkönen, "Optically pumped VECSELs: Review of technology and progress," *J. Phys. D: Appl. Phys.* **50**, 383001 (2017).
- ⁵C. A. Zaugg, A. Klenner, M. Mangold, A. S. Mayer, S. M. Link, F. Emaury, M. Golling, E. Gini, C. J. Saraceno, B. W. Tilma, and U. Keller, "Gigahertz self-referenceable frequency comb from a semiconductor disk laser," *Opt. Express* **22**, 16445 (2014).
- ⁶K. G. Wilcox, A. C. Tropper, H. E. Beere, D. A. Ritchie, B. Kunnert, B. Heinen, and W. Stolz, "4.35 kW peak power femtosecond pulse modelocked VECSEL for supercontinuum generation," *Opt. Express* **21**, 1599–1605 (2013).
- ⁷H. Lindberg, M. Strassner, E. Gerster, J. Bengtsson, and A. Larsson, "Thermal management of optically pumped long-wavelength InP-based semiconductor disk lasers," *IEEE J. Sel. Top. Quantum Electron.* **11**, 1126–1134 (2005).
- ⁸U. Keller and A. C. Tropper, "Passively modelocked surface-emitting semiconductor lasers," *Phys. Rep.* **429**, 67 (2006).
- ⁹M. L. Lukowski, C. Hessenius, J. T. Meyer, E. M. Wright, and M. Fallahi, "High power two-color orbital angular momentum beam generation using vertical external cavity surface emitting lasers," *Appl. Phys. Lett.* **112**, 041108 (2018).
- ¹⁰M. L. Lukowski, J. T. Meyer, C. Hessenius, E. M. Wright, and M. Fallahi, "Generation of high-power spatially structured beams using vertical external cavity surface emitting lasers," *Opt. Express* **25**, 25504 (2017).
- ¹¹H. A. Haus, "Mode-locking of lasers," *IEEE J. Sel. Top. Quantum Electron.* **6**, 1173–1185 (2000).
- ¹²S. V. Gurevich and J. Javaloyes, "Spatial instabilities of light bullets in passively-mode-locked lasers," *Phys. Rev. A* **96**, 023821 (2017).
- ¹³J. Hausen, S. Meinecke, B. Lingnau, and K. Lüdge, "Pulse cluster dynamics in passively mode-locked semiconductor vertical-external-cavity surface-emitting lasers," *Phys. Rev. Appl.* **11**, 044055 (2019).
- ¹⁴J. Mulet and S. Balle, "Mode-locking dynamics in electrically driven vertical-external-cavity surface-emitting lasers," *IEEE J. Quantum Electron.* **41**, 1148 (2005).
- ¹⁵J. Hader, M. Scheller, A. Laurain, I. Kilen, C. Baker, J. V. Moloney, and S. W. Koch, "Ultrafast non-equilibrium carrier dynamics in semiconductor laser mode-locking," *Semicond. Sci. Technol.* **32**, 013002 (2017).
- ¹⁶H. Haug and S. W. Koch, *Quantum Theory of the Optical and Electronic Properties of Semiconductors*, 4th ed. (World Scientific, 2004).
- ¹⁷A. Bäumer, S. W. Koch, and J. V. Moloney, "Non-equilibrium analysis of the two-color operation in semiconductor quantum-well lasers," *Phys. Status Solidi B* **248**, 843–846 (2011).
- ¹⁸A. Laurain, J. Hader, and J. V. Moloney, "Modeling and optimization of transverse modes in vertical-external-cavity surface-emitting lasers," *J. Opt. Soc. Am. B* **36**, 847 (2019).
- ¹⁹M. Brio, A. R. Zakharian, and G. M. Webb, in *Numerical Time-Dependent Partial Differential Equations for Scientists and Engineers*, edited by C. K. Chui (Mathematics in Science and Engineering, 2010), Vol. 213.
- ²⁰A. E. Siegman, in *Lasers*, edited by A. Kelly (University Science Books, California, 1986).